# Assessment of nonlinear flux assembly using central finite-difference methods in hyperbolic conservation laws

**By H. Song, H. Hwang AND P. Moin**

In numerical simulations of hyperbolic conservation laws using relatively coarse meshes, the solution often contains substantial spectral energy near the Nyquist wavenumber supported by the computational grid. Due to the limitations of numerical schemes, the dispersion relation in this high-wavenumber regime cannot be accurately represented. In addition, for nonlinear fluxes, aliasing errors are introduced during the flux assembly process. These numerical errors generate spurious fluctuations in the solution, which degrade the quality of the resolved solution structures and may ultimately lead to numerical instability. This work compares three flux assembly approaches for simulations using second-order and fourth-order finite-difference schemes. The results indicate that higher-order schemes exhibit improved capability in preserving solution structures. Furthermore, applying dealiasing treatments prior to nonlinear flux assembly is crucial, as it significantly reduces spurious fluctuations in the numerical solutions for both second-order and fourth-order schemes. The improvement is particularly effective for the second-order schemes.

## 1. Introduction

Eddy-resolving simulations are increasingly popular for studies of fundamental turbulence physics and engineering applications involving turbulent flows because of the balance of computational affordability and simulation fidelity. Grounded in the physics of turbulence, eddy-resolving simulations allow for partially resolved turbulence structures as fine as within the inertial subrange, along with modeling of effects of smaller-scale turbulent motions beyond the mesh resolution (Pope 2001). In the governing equations describing the dynamics of turbulent flows at resolvable length scales, nonlinear advection plays an important role. In many eddy-resolving simulations, to maximize solution quality, the dynamics of turbulent flows combined with coherent flow structures are computed over a wide range of length scales down to near grid size, where the closure model has dominant effects. This requirement poses significant challenges not only for the numerical schemes, which are responsible for maintaining accuracy at small scales, but also for the simulation framework, which can handle nonlinear interactions across a broad spectrum of turbulent length scales under constrained mesh resolution.

In the numerical solution of partial differential equations using finite-difference methods, the error due to spatial discretization decreases with mesh refinement at a rate consistent with the formal order of convergence of the numerical schemes employed. This asymptotic convergence occurs when the solution is numerically well-resolved by the computational mesh. However, when the computational mesh is insufficient to resolve the solution to the governing equations down to the smallest scales, the analysis of the leading-order truncation error of numerical schemes is invalid. From the perspective

of spectral analysis (Lele 1992; Song *et al.* 2024), the formal order of convergence represents the spectral behavior, such as the modified wavenumber and transfer function, near the limit when the wavenumber approaches zero. In practice, the numerical error is jointly influenced by the spectral energy distribution of the exact solution and the collective spectral response of the numerical schemes involved (Ghate & Lele 2023). In this regime, the numerical error is not guaranteed to show asymptotic convergence with mesh refinement.

In simulations of nonlinear governing partial differential equations, aliasing error arising from nonlinear interactions can lead to spurious energy transfer across scales. In partially resolved simulations, such errors can undermine solution accuracy at small scales and potentially induce numerical instability during time integration. Conceptually, the most effective approach to controlling aliasing error is to eliminate aliased modes during the evaluation of nonlinear interactions. For multiplicative interactions, aliasing error can be entirely removed (Orszag 1971). However, in more general cases, although there is no efficient way to completely remove aliasing error, it can be greatly reduced (Pirozzoli 2010, 2011; Song *et al.* 2022, 2024).

For individual numerical schemes used for simulations, the capability of resolving the flow structures at small scales can be achieved by improving the spectral resolution (Mansour *et al.* 1979; Lele 1992; Nagarajan *et al.* 2003). However, in the absence of dealiasing, numerical schemes with higher spectral resolution tend to generate larger aliasing errors. Consequently, the simulation framework should preserve high spectral resolution for the leading-order linear dynamics of the governing equations while efficiently reducing aliasing errors in nonlinear interactions.

For simulations of compressible turbulent flows, Song *et al.* (2022, 2024) propose to interpolate primitive variables prior to assembly of nonlinear fluxes at the edge-staggered grid points. In addition, they demonstrate that this approach can effectively mitigate aliasing error in the advective fluxes to achieve numerical solutions with high spectral resolution relative to the computational mesh, and the simulations using high-order compact finite-difference methods can be stabilized without applying solution filtering. However, for simulations using lower-order explicit schemes, the simulation can preserve robustness for various approaches to assembling nonlinear fluxes. This research brief presents an assessment of various nonlinear flux assembly approaches using explicit finite-difference methods. The numerical schemes and the different approaches to flux assembly are described in Section 2. The effects of the candidate flux assembly approaches are first compared in the Burgers system, and the results are illustrated in Section 3. Section 4 extends the comparison to homentropic flows by solving the two-dimensional Euler system.

## 2. Mathematical background

Let $\phi(\boldsymbol{x}, t)$ be a conservative variable, where $\boldsymbol{x}$ and $t$ are the spatial coordinate and time in the Eulerian frame, respectively. The strong conservation law that governs the evolution of $\phi$ can be formulated as follows,

$$\frac{\partial \phi}{\partial t} + \nabla \cdot \boldsymbol{\mathcal{F}}(\phi) = 0, \tag{2.1}$$

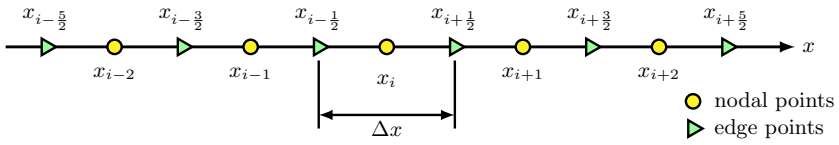


where $\boldsymbol{\mathcal{F}}(\phi)$ is the flux. For simplicity, the discussion is temporally reduced to one dimension. Correspondingly, Eq. (2.1) can be expressed in the following form,

$$\frac{\partial \phi}{\partial t} + \frac{\partial \mathcal{F}}{\partial x} = 0. \tag{2.2}$$

Equation (2.2) can be partially discretized in space, and the spatial derivative, $\partial_x \phi$, is evaluated using a discrete differential operator. As a result, Eq. (2.2) becomes an algebraic differential equation and can be denoted as

$$\frac{d\phi}{dt} + \frac{1}{\Delta x}\mathcal{D}_p \phi = \mathcal{O}(\Delta x^p), \tag{2.3}$$

where $\Delta x$ is the grid spacing resulting from the spatial discretization. The computational grid is assumed to be uniform. $\mathcal{D}_p$ represents an undivided finite-difference operator with formally $p$th-order accuracy. The right-hand side of Eq. (2.3) represents the truncation error. The definition of $\mathcal{D}_p$ is not unique. Different schemes have unique spectral behavior. Additionally, the leading-order truncation error may differ, although the schemes have the same formal order of convergence (Lele 1992).

For a conservative discretization, Eq. (2.3) yields the flux-difference form,

$$\left.\frac{d\phi}{dt}\right|_{x_i} + \frac{\widehat{\mathcal{F}}_{i+1/2} - \widehat{\mathcal{F}}_{i-1/2}}{\Delta x} = \mathcal{O}\left(\Delta x^p\right), \tag{2.4}$$

where $x_i$ represents the $i$th nodal point corresponding to the computational mesh, and the subscripts $i + 1/2$ and $i - 1/2$ represent the neighboring-edge staggered points of $x_i$ at $x_i + \Delta x/2$ and $x_i - \Delta x/2$, respectively. Figure 2 shows a schematic of one-dimensional discretization. The overhat $\widehat{(\cdot)}$ denotes that the quantity is reconstructed for the difference operation. The reconstruction can be considered a split operator of $\mathcal{D}_p$,

$$\mathcal{D}_p = \mathcal{D}_2 \mathcal{R}_p, \tag{2.5}$$

where $\mathcal{R}_p$ is a reconstruction operator with formal order of $\mathcal{O}(\Delta x^p)$, and $\mathcal{D}_2$ represents the calculation of flux difference shown in Eq. (2.4). According to the derivation, the reconstructed flux $\widehat{\mathcal{F}}$ differs from the exact flux $\mathcal{F}$ by $\mathcal{O}(\Delta x^2)$, regardless of the reconstruction order $p$; that is, $\widehat{\mathcal{F}} = \mathcal{F} + \mathcal{O}(\Delta x^2)$. The higher-order accuracy of the reconstruction operator $\mathcal{R}_p$, for $p > 2$, is realized only after applying the difference operator, which is equivalent to a $\mathcal{D}_2$ operator. In addition to enforcing discrete conservation, in simulations of compressible flows using finite-difference methods, the flux-difference form in Eq. (2.4) is favored when the schemes are locally blended with nonlinear interpolation or reconstruction schemes for shock capturing (Shu 2009) and when a positivity-preserving limiter is needed (as in Subramaniam *et al.* 2019, Wong *et al.* 2021).

On the basis of the spatial relationship between input and output data, finite-difference operators can be classified into two categories: collocated and staggered operators. In collocated operators, the output is evaluated at the same grid locations as the input data. In contrast, staggered operators produce output at positions offset by half a grid spacing, which are staggered relative to the input locations. According to this classification, the

flux-difference operation in Eq. (2.4) is staggered. Assuming that the time integration of conservative variables is at the nodal grid points, the overall operation to obtain the reconstructed fluxes to conduct the flux-difference operation is staggered. For a hyperbolic conservation system, the flux can be treated as an arithmetic operation of the conservative variables. Correspondingly, there are generally two ways to obtain the reconstructed fluxes at the edge-staggered grid points.

One of these approaches involves directly assembling the fluxes at the edge grid points. Because the conservative variables are initially unavailable at the edge points, numerical interpolation schemes need to be applied. Therefore, the numerical flux is calculated as $\mathcal{F}(\mathcal{I}_p\phi)$, where $\mathcal{I}_p$ denotes a midpoint interpolation scheme with a leading-order truncation error of $\mathcal{O}(\Delta x^p)$. Correspondingly, the reconstruction operator $\mathcal{R}_p$ is collocated in order to satisfy the flux-difference operation. The second approach involves assembling fluxes at nodal points and interpolating the fluxes to the edge points. In association with this approach, the flux operator $\mathcal{F}$ is collocated, and the reconstruction operator can be either collocated, as used in the previous approach along with an interpolation operator (i.e., $\widehat{\mathcal{F}} = \mathcal{R}_p^{\text{coll}}\mathcal{I}_p\mathcal{F}(\phi)$), or staggered as a fusion of interpolation and collocated reconstruction (i.e., $\mathcal{R}_p^{\text{stag}} = \mathcal{R}_p^{\text{coll}}\mathcal{I}_p$); here, the superscripts coll and stag denote subsets of the schemes that are collocated and staggered, respectively. Furthermore, subject to the collocated derivative operator, $\mathcal{D}_p^{\text{coll}}$, a staggered reconstruction operator, $\mathrm{R}_p^{\text{stag}}$, can also be formulated. This concept is mathematically consistent with the fused reconstruction operator, $\mathcal{R}_p^{\text{coll}}\mathcal{I}_p$, but the expression of $\mathcal{R}_p^{\text{stag}}$ is different. The concept of $\mathcal{R}_p^{\text{stag}}$ has been widely used in the finite-difference-weighted-essentially-nonoscillatory schemes that contain additional convex nonlinear superpositions of the candidate linear results (Shu 2009). Note that for specific problems, especially when the fluxes are nonlinear, both approaches can develop many variations of detailed implementation for numerical accuracy and robustness.

This study assesses the accuracy of the two flux assembly approaches in finite-difference computational frameworks using second-order and fourth-order central schemes. Under these conditions, a general expression of collocated central differential operators is

$$\frac{1}{\Delta x}\,\mathcal{D}_p^{\text{coll}}\phi\big|_{x_i} = a\frac{\phi_{i+1}-\phi_{i-1}}{2\Delta x} + (1-a)\frac{\phi_{i+2}-\phi_{i-2}}{4\Delta x}, \tag{2.6}$$

and the corresponding staggered reconstruction method is

$$\mathcal{R}_p^{\text{stag}}\phi\big|_{x_i} = \frac{1+a}{4}\left(\phi_{i+\frac{1}{2}}+\phi_{i-\frac{1}{2}}\right) + \frac{1-a}{4}\left(\phi_{i+\frac{3}{2}}+\phi_{i-\frac{3}{2}}\right). \tag{2.7}$$

A general expression of staggered central differential operators is

$$\frac{1}{\Delta x}\,\mathcal{D}_p^{\text{stag}}\phi\big|_{x_i} = a\frac{\phi_{i+\frac{1}{2}}-\phi_{i-\frac{1}{2}}}{\Delta x} + (1-a)\frac{\phi_{i+\frac{3}{2}}-\phi_{i-\frac{3}{2}}}{3\Delta x}, \tag{2.8}$$

and the corresponding collocated reconstruction is

$$\mathcal{R}_p^{\text{coll}}\phi\big|_{x_i} = \frac{1-a}{3}\phi_{i-1} + \frac{1+2a}{3}\phi_i + \frac{1-a}{3}\phi_{i+1}. \tag{2.9}$$

A general expression of central interpolation schemes is

$$\mathcal{I}_p\phi\big|_{x_i} = \frac{a}{2}\left(\phi_{i+\frac{1}{2}}+\phi_{i-\frac{1}{2}}\right) + \frac{1-a}{2}\left(\phi_{i+\frac{3}{2}}+\phi_{i-\frac{3}{2}}\right). \tag{2.10}$$

All the schemes given in Eqs. (2.6)-(2.10) are formally second-order accurate with a coefficient $a$. When $a = 0$, the schemes have the most compact stencils to maintain

| Schemes | Reference Solution | $a_4$ | Truncation Error |
|---|---|---|---|
| Eqs. (2.6), (2.7) | $\partial\phi/\partial x$ | 4/3 | $\left(\frac{2}{3}-\frac{1}{2}a\right)\frac{\partial^3\phi}{\partial x^3}\Delta x^2+\left(\frac{2}{15}-\frac{1}{8}a\right)\frac{\partial^5\phi}{\partial x^5}\Delta x^4+\mathcal{O}\left(\Delta x^6\right)$ |
| Eqs. (2.8), (2.9) | $\partial\phi/\partial x$ | 9/8 | $\left(\frac{3}{8}-\frac{1}{3}a\right)\frac{\partial^3\phi}{\partial x^3}\Delta x^2+\left(\frac{1}{1920}+\frac{1}{24}a\right)\frac{\partial^5\phi}{\partial x^5}\Delta x^4+\mathcal{O}\left(\Delta x^6\right)$ |
| Eq. (2.10) | $\phi$ | 9/8 | $\left(\frac{9}{8}-a\right)\frac{\partial^2\phi}{\partial x^2}\Delta x^2+\left(\frac{27}{128}-\frac{5}{24}a\right)\frac{\partial^4\phi}{\partial x^4}\Delta x^4+\mathcal{O}\left(\Delta x^6\right)$ |

TABLE 1. Truncation errors of the central schemes provided in Eqs.(2.6)-(2.10), where $a_4$ is the specific value of $a$ for each scheme to achieve fourth-order accuracy, and the truncation error is defined as the reference solution subtracted from the numerical solution.

second-order accuracy. For each scheme, a specific value of $a$ will cause the leading-order truncation error to vanish, and the scheme will become formally fourth-order accurate. Table 1 lists the values of $a$ for the schemes and their associated truncation error.

This study compares the effects of three different flux assembly and reconstruction methods, and all methods are subjected to the flux-difference form to evaluate the divergence of the flux. The three methods are as follows, assuming that the conservative variable $\phi$ is initially available at the nodal points.

In Method 1, $\widehat{\mathcal{F}}=\mathcal{R}_p^{\text{stag}}\mathcal{F}(\phi)$, the flux is assembled at the nodal points first, and a staggered reconstruction is applied on the basis of Eq. (2.7). This method is equivalent to the collocated finite-difference approach using Eq. (2.6).

In Method 2, $\widehat{\mathcal{F}}=\mathcal{R}_p^{\text{coll}}\mathcal{I}_p\mathcal{F}(\phi)$, the flux is assembled at the nodal points and interpolated to the edge points according to Eq. (2.10). A collocated reconstruction based on Eq. (2.9) is then applied. The collocated construction is subjected to the staggered finite-difference approach using Eq. (2.8). In this method, the specific formulation of the equivalent fused operator, $\mathcal{R}_p^{\text{coll}}\mathcal{I}_p$, differs from $\mathcal{R}_p^{\text{stag}}$ used in Method 1.

In Method 3, $\widehat{\mathcal{F}}=\mathcal{R}_p^{\text{coll}}\mathcal{F}(\mathcal{I}_p\phi)$, the primitive variable (if different from the conservative variable) is interpolated from the nodal points to the edge points. The flux is assembled using the interpolated primitive variables. A collocated flux reconstruction based on Eq. (2.7) is then applied at the edge points subjected to the staggered finite-difference approach using Eq. (2.8).

For each method, the numerical schemes are based on the second-order formulations with the most compact stencils (i.e., $a=1$) and the fourth-order formulations, respectively. Based on the analysis by Song *et al.* (2024), for linear fluxes, the collective truncation errors of Method 1 and Method 2 are both

$$\frac{1}{6}\frac{\partial^3\phi}{\partial x^3}\Delta x^2+\mathcal{O}\left(\Delta x^4\right)$$

using the second-order schemes, and the spectral analysis shows that truncation errors are the same in all higher-order terms included in $\mathcal{O}\left(\Delta x^4\right)$ as well. Therefore, while using the second-order schemes (i.e., $a=1$), Methods 1 and 2 collapse. The collective truncation errors using the fourth-order schemes are

$$-\frac{1}{30}\frac{\partial^5\phi}{\partial x^5}\Delta x^4+\mathcal{O}\left(\Delta x^6\right)\quad\text{and}\quad-\frac{9}{320}\frac{\partial^5\phi}{\partial x^5}\Delta x^4+\mathcal{O}\left(\Delta x^6\right)$$

for Methods 1 and 2, respectively. For nonlinear fluxes, Methods 1 and 2 do not contain any dealiasing treatment, while Method 3 implicitly contains a dealiasing treatment prior

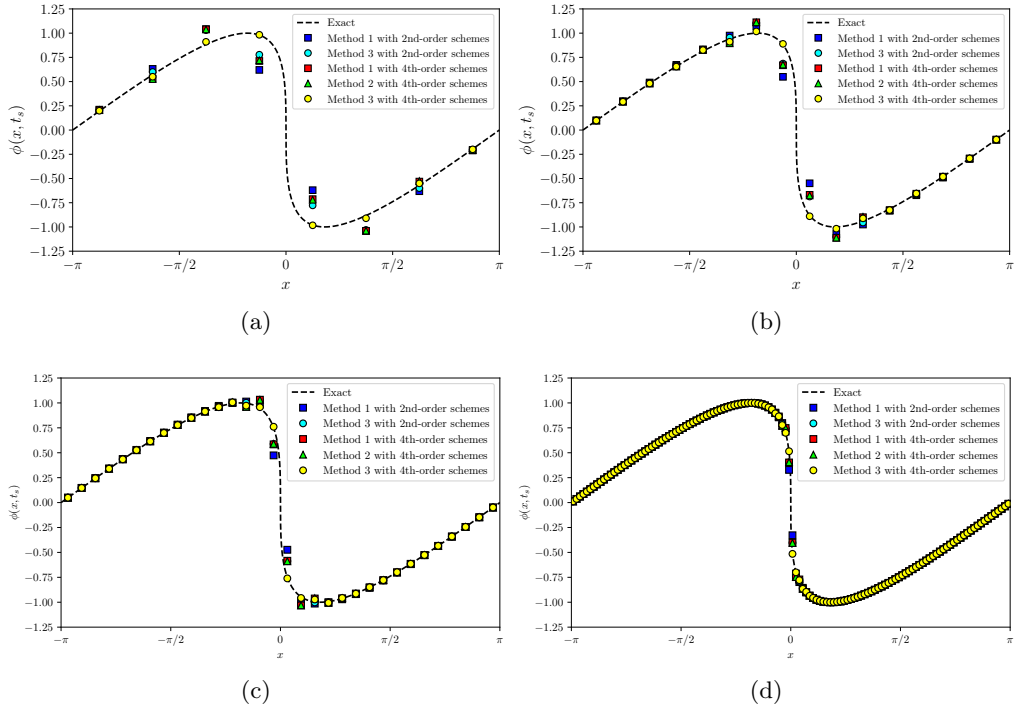


FIGURE 1. Visualization of the numerical solutions to the Burgers equation at $t_s$ with different mesh sizes $N$: (a) $N = 8$, (b) $N = 16$, (c) $N = 32$, and (d) $N = 128$.

to flux assembly due to the spectral property of the central interpolation schemes (Song *et al.* 2022, 2024; Ghate & Lele 2023).

## 3. Solutions to the Burgers equation

In this section, the Burgers equation is used for the assessment. The Burgers equation is formulated in one-dimensional space as

$$\frac{\partial \phi}{\partial t} + \frac{\partial}{\partial x}\left(\frac{\phi^2}{2}\right) = 0. \tag{3.1}$$

The Burgers equation is commonly used as a model equation to study nonlinear transport. In addition, it can be treated as a prototype equation for studying nonlinear compression, analogous to the formulation of an artificial compression method as a modeled interface-sharpening mechanism for simulations of multiphase flows (Saurel & Pantano 2018). In the Burgers equation, the nonlinearity in the flux is due to the quadratic interaction of the variable $\phi$. The simulations are deployed on a periodic domain for $x \in [-\pi, \pi)$. The initial condition is set to be

$$\phi_0(x) = -\sin(x). \tag{3.2}$$

Under this initial condition, for $t > 0$, the profile of $\phi$ is compressed toward $x = 0$ from both sides, and the solution will develop a shock at $x = 0$ at $t_s = 1$. At the shock formation time $t_s$, the slope of the solution profile $\partial\phi/\partial x$ contains one singularity at $x = 0$, but the solution remains smooth elsewhere. For $t \in [0, t_s]$, the Burgers system has

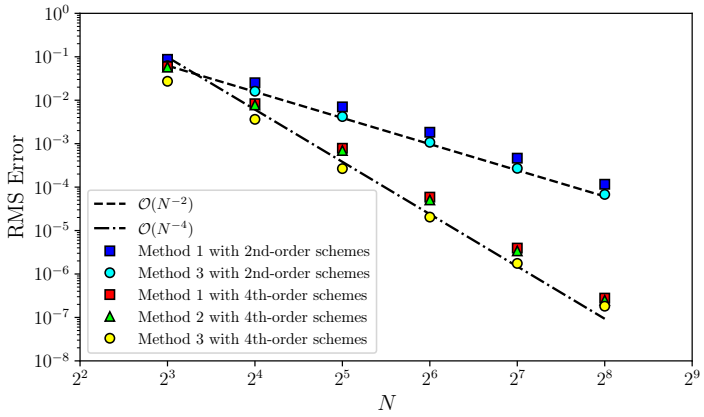


FIGURE 2. Grid convergence measurements of the numerical solution to the Burgers equation at $t = t_s/2$.

the following analytical solution, provided in an implicit form,

$$\phi = \sin(\phi t - x). \tag{3.3}$$

For spatial discretization, the nodal points are located at $x_i = 2\pi(i + 1/2)/N - \pi$ for $i = 0, 1, 2, \ldots, N-1$. For an even number $N$, no nodal point is located at the singularity position at $t_s$. For comparison, the time integration method for all simulations is the third-order strong-stability-preserving Runge–Kutta method (SSP-RK3) (Shu & Osher 1988) with the Courant–Friedrichs–Lewy (CFL) number fixed at 0.5, except for the last time step.

The numerical solutions at $t = t_s$ obtained using the three different flux assembly methods (see Section 2) with second-order and fourth-order schemes are shown in Figure 1. Because $t_s$ is the shock formation time, and the exact solution contains a singularity, all numerical solutions are underresolved at $x = 0$. Accordingly, the Gibbs phenomenon is expected, and all the numerical solutions close to $x = 0$ exhibit first-order accuracy at $t_s$ (Moin 2010). Nevertheless, all numerical solutions asymptotically converge as the computational mesh is refined. As shown in Figure 1, although all numerical solutions exhibit the Gibbs phenomenon, the solution obtained with Method 3 employing the fourth-order scheme shows the most reduced spurious oscillations compared with the other methods and schemes. This advantage becomes more noticeable under coarser mesh conditions, as depicted in Figure 1(a,b). For extremely underresolved simulations, where a substantial portion of the spectral energy of the reference solution lies beyond the Nyquist wavenumber supported by the computational mesh, the resulting aliasing error becomes pronounced. Among all the simulations, the one using Method 3 with fourth-order schemes benefits from both the lower truncation error arising from higher-order schemes in the linear regime and the smaller aliasing error via the central interpolation scheme in the nonlinear regime.

The grid convergence of different methods and schemes is shown in Figure 2 for values of $N$ from 8 to 256. Compared with the reference lines, all methods can achieve the formal order of convergence associated with mesh refinement. For Method 3 at each order of schemes, the numerical error is consistently lower compared with Methods 1 and 2, even though Method 1 has the lowest absolute value of the truncation error in the linear regime. This behavior further suggests that a reduced aliasing error contributes to

under-resolved simulations of nonlinear systems. The difference between the measured numerical errors of Methods 1 and 2 is small, as shown in Figure 2. This behavior is consistent with the analytical demonstration that the spectral behavior of the truncation errors and the leading-order truncation errors (cf. Section 2) between the two methods are small (Song *et al.* 2024).

## 4. Simulations of homentropic flows

In this section, the assessment is applied to compressible Euler equations. The system equations govern the compressible inviscid flows, including the conservation of mass, momentum, and total energy, as follows,

$$\frac{\partial \rho}{\partial t} + \nabla \cdot (\rho \boldsymbol{u}) = 0, \tag{4.1}$$

$$\frac{\partial \rho \boldsymbol{u}}{\partial t} + \nabla \cdot (\rho \boldsymbol{u} \otimes \boldsymbol{u} + p\mathbb{I}) = 0, \tag{4.2}$$

$$\frac{\partial \rho e}{\partial t} + \nabla \cdot (\rho h \boldsymbol{u}) = 0, \tag{4.3}$$

where $\rho$ is the density; $\boldsymbol{u}$ is the velocity vector; $p$ is the pressure; $e$ is the specific total energy; and $h$ is the specific total enthalpy, $h = e + p/\rho$. The system is closed by the equation of state for a calorically perfect gas,

$$\frac{p}{\gamma - 1} = \rho \left( e - \frac{\boldsymbol{u} \cdot \boldsymbol{u}}{2} \right), \tag{4.4}$$

where $\gamma$ is a constant representing the ratio of specific heats. In this section, $\gamma = 1.4$ is used for all simulations. In the Euler system, the fluxes are highly nonlinear beyond multiplicative operations.

The demonstrative application is the advection of a homentropic swirl on a two-dimensional periodic domain (Visbal & Gaitonde 2002; Kawai & Lele 2008; Nonomura *et al.* 2010; Song *et al.* 2022, 2024). The simulation configurations are set according to the conditions used by Song *et al.* (2024). The computational domain spans a two-dimensional space for $(x, y) \in [-6, 6)^2$, and the domain is periodic in each dimension. The advection is carried by a uniform flow as the base state at a Mach number of 0.5. The swirl is imposed on the uniform base state as a homentropic perturbation, described in a consistent polar coordinate system as follows,

$$\begin{cases} \delta \boldsymbol{u} = \epsilon r e^{\alpha\left(1-r^2\right)} \hat{\boldsymbol{e}}_l(\theta), \\ \delta T = -\epsilon^2 \frac{\gamma - 1}{4R\alpha\gamma} e^{2\alpha\left(1-r^2\right)}, \end{cases} \tag{4.5}$$

where $r$ and $\theta$ are the radius and polar angle, respectively; $\delta$ denotes a perturbed component of a quantity; $T$ represents the temperature; $\epsilon = 0.3$ represents an inverse of the timescale and characterizes the perturbation amplitude; $\alpha$ characterizes the size of the swirl, and $\alpha = 1.2$ is set to ensure sufficient decay of the perturbation to maintain numerically smooth perturbation fields over the periodic domain; $\hat{\boldsymbol{e}}_l = \hat{\boldsymbol{e}}_x \sin\theta - \hat{\boldsymbol{e}}_y \cos\theta$ denotes the unit vector tangent to the circle centered at the origin; and $R$ is the specific gas constant, which is set to unity, $R = 1$. For a calorically perfect gas, the pressure–density–temperature relation yields the ideal-gas law, $p = \rho R T$, and the speed of sound is calculated as $\sqrt{\gamma p/\rho}$. For the homentropic flow, $p/\rho^\gamma$ remains constant. In this homen-

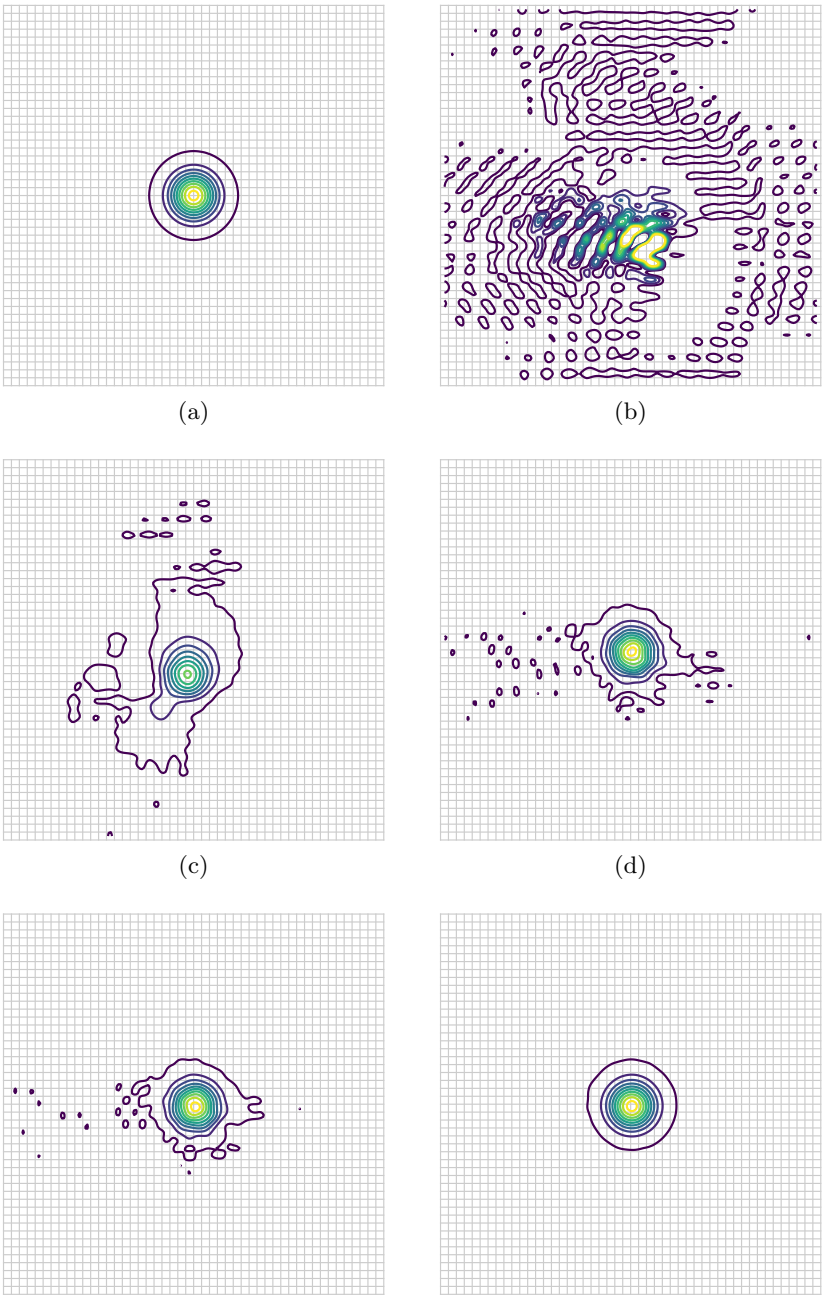

FIGURE 3. Visualization of the normalized pressure field, $(p - p_\infty)/\delta p_{00}$, after one advection period, where $p_\infty$ is the base-state pressure and $\delta p_{00}$ is the perturbation pressure at the origin in the initial flow state. The contours uniformly span from $-0.01\delta p_{00}$ to $-0.95\delta p_{00}$. The results are upsampled for visualization purposes only. (a) Reference solution. (b) Method 1 with second-order schemes. (c) Method 3 with second-order schemes. (d) Method 1 with fourth-order schemes. (e) Method 2 with fourth-order schemes. (f) Method 3 with fourth-order schemes.

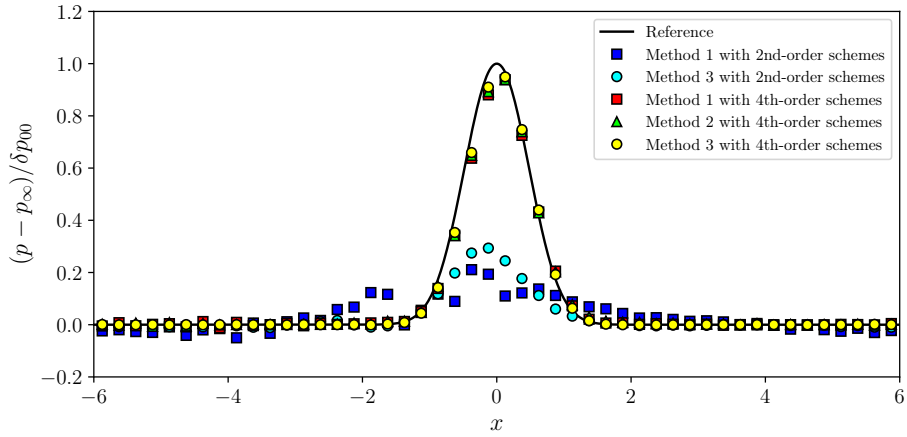


FIGURE 4. Centerline pressure profiles at $y = 0$ after one advection period.

tropic flow, after each advection period, the flow fields should be the same as in the initial conditions. Therefore, the initial conditions can also serve as the reference solution.

The computational domain is uniformly discretized with $N = 48$ grid points in both the $x$ and $y$ dimensions. This mesh size, $N$, is larger than that used by Song *et al.* (2024). A coarser mesh, $N = 32$, is used in Song *et al.* (2024). The time advancement is conducted using the SSP-RK3 scheme at a constant CFL number of 0.5. The flow is simulated up to one advection period. Under these configurations, all simulations (see Section 2) result in numerically stable solutions. At the final stage, the perturbation pressure fields from different simulations are depicted in Figure 3, where Figure 3(a) is the initial condition and also serves as the reference solution. The perturbation pressure is normalized by the maximum perturbation, which is at the origin, in the initial condition. The centerline pressure profiles at $y = 0$ for all simulations are plotted in Figure 4.

Based on the reference solution, the mesh resolution is relatively coarse for resolving the flow feature. The Gaussian profile is resolved approximately by 12 grid points. As shown in Figures 3 and 4, the fourth-order schemes yield solutions that better preserve the flow structures under these flow configurations. Compared with the second-order schemes, the fourth-order schemes demonstrate improved accuracy in resolving the peak values of the solutions. Among the schemes with the same formal order accuracy, Method 3 with implicit dealiasing via the central interpolation schemes exhibits noticeable advantages in reducing spurious fluctuations in the numerical solutions. This benefit improves the solution quality for both second-order and fourth-order schemes.

## 5. Concluding remarks

Three methods for flux assembly in finite-difference simulations are identified for assessment of their numerical performance in hyperbolic conservation systems. The divergence of the flux is calculated using a central derivative scheme, and the corresponding reconstruction scheme is derived to satisfy the flux-difference form. In Methods 1 and 2, the fluxes are assembled at collocated nodal points. For nonlinear fluxes, the flux assembly does not include dealiasing treatment. In Method 3, the fluxes are assembled at staggered edge points using the interpolated primitive variables. For nonlinear fluxes, implicit dealiasing can be achieved through the spectral properties of the central interpolation

schemes. The three methods are applied with the corresponding second-order and fourth-order schemes to solve a Burgers equation and the compressible Euler equations. In both demonstrative applications, fourth-order schemes exhibit improved quality in preserving detailed flow features compared with second-order schemes. Among the numerical schemes that have the same formal order of accuracy, Method 3, which has a dealiasing treatment, effectively reduces spurious fluctuations in the numerical solutions for both second-order and fourth-order schemes in comparison to Methods 1 and 2, which do not include dealiasing.

*Acknowledgments*

The authors are grateful to Prof. Sanjiva K. Lele, Lucy J. Brown, and Dr. Alexander N. W. Cicchino from the Center for Turbulence Research for helpful comments and discussions. Support from the Office of Naval Research to the Center for Turbulence Research (grant N000142312833) is gratefully acknowledged.

## REFERENCES

Ghate, A. & Lele, S. K. 2023 Finite difference methods for turbulence simulations. In *Numerical Methods in Turbulence Simulation*, pp. 235–284. Elsevier.

Kawai, S. & Lele, S. K. 2008 Localized artificial diffusivity scheme for discontinuity capturing on curvilinear meshes. *J. Comput. Phys.* **227**, 9498–9526.

Lele, S. K. 1992 Compact finite difference schemes with spectral-like resolution. *J. Comput. Phys.* **103**, 16–42.

Mansour, N., Moin, P., Reynolds, W. & Ferziger, J. 1979 Improved methods for large eddy simulations of turbulence. In *Turbulent Shear Flows I: Selected Papers from the 1st International Symposium on Turbulent Shear Flows* (ed. F. Durst, B. Launder, F. Schmidt & J. Whitelaw), pp. 386–401. Springer.

Moin, P. 2010 *Fundamentals of Engineering Numerical Analysis*. Cambridge University Press.

Nagarajan, S., Lele, S. K. & Ferziger, J. H. 2003 A robust high-order compact method for large eddy simulation. *J. Comput. Phys.* **191**, 392–419.

Nonomura, T., Iizuka, N. & Fujii, K. 2010 Freestream and vortex preservation properties of high-order WENO and WCNS on curvilinear grids. *Comput. Fluids* **39**, 197–214.

Orszag, S. A. 1971 On the elimination of aliasing in finite-difference schemes by filtering high-wavenumber components. *J. Atmos. Sci.* **28**, 1074.

Pirozzoli, S. 2010 Generalized conservative approximations of split convective derivative operators. *J. Comput. Phys.* **229**, 7180–7190.

Pirozzoli, S. 2011 Stabilized non-dissipative approximations of Euler equations in generalized curvilinear coordinates. *J. Comput. Phys.* **230**, 2997–3014.

Pope, S. B. 2001 Turbulent flows. *Meas. Sci. Technol.* **12**, 2020–2021.

Saurel, R. & Pantano, C. 2018 Diffuse-interface capturing methods for compressible two-phase flows. *Annu. Rev. Fluid Mech.* **50**, 105–130.

Shu, C.-W. 2009 High order weighted essentially nonoscillatory schemes for convection dominated problems. *SIAM Rev.* **51**, 82–126.

Shu, C.-W. & Osher, S. 1988 Efficient implementation of essentially non-oscillatory shock-capturing schemes. *J. Comput. Phys.* **77**, 439–471.

Song, H., Ghate, A. S., Matsuno, K., West, J., Subramaniam, A., Brown, L. J. & Lele, S. K. 2022 Robust high-resolution simulations of compressible turbulent flows without filtering. *AIAA Paper 2022-4122* .

Song, H., Ghate, A. S., Matsuno, K. V., West, J. R., Subramaniam, A. & Lele, S. K. 2024 A robust compact finite difference framework for simulations of compressible turbulent flows. *J. Comput. Phys.* **519**, 113419.

Subramaniam, A., Wong, M. L. & Lele, S. K. 2019 A high-order weighted compact high resolution scheme with boundary closures for compressible turbulent flows with shocks. *J. Comput. Phys.* **397**, 108822.

Visbal, M. R. & Gaitonde, D. V. 2002 On the use of higher-order finite-difference schemes on curvilinear and deforming meshes. *J. Comput. Phys.* **181**, 155–185.

Wong, M. L., Angel, J. B., Barad, M. F. & Kiris, C. C. 2021 A positivity-preserving high-order weighted compact nonlinear scheme for compressible gas-liquid flows. *J. Comput. Phys.* **444**, 110569.